


Compensation of Anisotropy in Spin Hall Devices for Neuromorphic Applications

Pankaj Sethi^{Ⓧ,*†}, Dédalo Sanz-Hernández[Ⓧ], Florian Godel, Sachin Krishnia, Fernando Ajejas^{Ⓧ,‡},
Alice Mizrahi, Vincent Cros[Ⓧ], Danijela Marković, and Julie Grollier

Unité Mixte de Physique CNRS/Thales, Université Paris-Saclay, 91767 Palaiseau, France

 (Received 12 January 2023; revised 29 March 2023; accepted 10 May 2023; published 6 June 2023)

Spintronic nano-oscillators and diodes with reduced nonlinearity benefit from low phase noise and improved device properties. Moreover, they could offer key advantages for realizing neuromorphic applications, such as spike-based neurons and frequency multiplexing in neural networks. Here, we experimentally demonstrate the reduction in nonlinearity of a spin Hall nano-oscillator (SHNO) by compensation of its effective magnetic anisotropy. The study involves optimization of Co/Ni multilayer growth to achieve the compensation, followed by spin-diode measurements on patterned microstrips to quantify their anisotropy. The relationship between the second- ($H_{k_2} = 0.47$ mT) and first-order ($H_{k_1}^{\text{eff}} = -0.8$ mT) anisotropy fields reveals the existence of an easy cone, thereby validating the presence of compensation. Furthermore, we demonstrate a compensated spin diode that has a fixed frequency when the input power is varied. We then study the current-induced auto-oscillation properties of SHNOs on compensated films by patterning nanoconstrictions of 200 and 100 nm wide. The invariance of the resonance frequency and linewidth of the compensated SHNO with applied dc current indicates the absence of nonlinearity. This independence is maintained irrespective of the applied external fields and their orientations. The compensated SHNO obtained has a linewidth of 1.1 MHz and a peak output power of up to 1 pW/MHz.

DOI: [10.1103/PhysRevApplied.19.064018](https://doi.org/10.1103/PhysRevApplied.19.064018)

I. INTRODUCTION

Spintronic nano-oscillators are nanoscale microwave generators that undergo auto-oscillations when the spin transfer or spin-orbit torque, due to the applied dc current, counteracts damping due to magnetization precession [1–4]. Nonlinearity is prevalent in the magnetization dynamics of such nano-oscillators. In a nonlinear auto-oscillator, the frequency, f , has a component that depends on the precession amplitude or the effective magnetization given by

$$f = f_{\text{FMR}} + Np, \quad (1)$$

where f_{FMR} is the frequency at ferromagnetic resonance, N is the nonlinear frequency shift coefficient, and p is the term related to the amplitude of precession [5,6]. It is worth noting that, even in the complete absence of nonlinearity ($N = 0$), the frequency of the oscillators can still be offset from f_{FMR} on account of internal fields. These internal fields can arise, for instance, due to the device geometry, as demonstrated in Ref. [7] for spin Hall oscillators

based on nanoconstriction geometries. The nonlinear frequency shift, N , emerges from an effective anisotropy in the system, which results in a noncircular trajectory of the precessing magnetization. The magnetization dynamics in the ferromagnetic layer are inherently nonlinear due to the nonlinear relationship between the applied magnetic field, magnetization, and resulting precession frequency. This nonlinearity affects the frequency response of the spintronic nano-oscillator, causing it to depend on the precession amplitude [6]. It leads to a large frequency tunability with current, which provides multifunctionality to these nano-oscillators, such as the possibility to be modulated or synchronized [8–10]. This is exploited in realizing numerous applications relevant to data communication [11–15] and neuromorphic computing [16–19]. However, there are certain systems where it is possible to reduce the effective anisotropy and, as a result, the nonlinearity. In such compensated systems, the anisotropy field is counterbalanced by the demagnetization field, resulting in circular trajectories of the precessing magnetization [20]. The absence of nonlinearity, which results in a constant frequency with respect to the injected input power or current, also offers key benefits for realizing neuromorphic applications. For instance, multiply-and-accumulate (MAC) operations using spintronic resonators employ frequency multiplexing to uniquely address input radio-frequency (rf) signals from neurons to the corresponding resonators [21,22]. This requires the neurons and corresponding spin-diode-based

*pankaj8684@gmail.com

†pankaj.sethi@cnrs-thales.fr

‡Present address: Department of Physics and Center for Advanced Nanoscience, University of California, San Diego, La Jolla, California, 92093, USA

synapses to resonate at a relatively fixed frequency independent of the injected rf power. Here, we show that fixed-frequency operation can be accomplished by compensating for anisotropy in spintronic nano-oscillators and spin diodes, respectively. Second, an absence of nonlinearity can reduce the phase noise of the nano-oscillator by removing the effect of amplitude noise on it. The linewidth, Δf , of an auto-oscillator, which is a measure of its phase noise [23] is given by

$$\Delta f = \Delta f_{\text{thermal}}(1 + N^2/\Gamma_{\text{eff}}^2), \quad (2)$$

where $\Delta f_{\text{thermal}}$ is the contribution from the thermal generation linewidth and Γ_{eff} is the effective damping [5]. The second term, which is the contribution from the amplitude noise, can be neglected if N is very small. Another application is the realization of spike-based neurons, as recently demonstrated via a macrospin approach and micromagnetic simulations [24]. It is shown that anisotropy compensation in a spin Hall geometry results in circular trajectories of the precessing magnetization, and the resulting output is a chain of spikes emulating biological neurons. Thus, it is important to study systems with compensated anisotropy.

Recently, Jiang *et al.* demonstrated a linewidth reduction of spin-valve-based spin-torque nano-oscillators (STNOs) by controlling the perpendicular magnetic anisotropy (PMA) of their films using He-ion irradiation [25]. An alternative planar geometry based on heavy-metal and ferromagnetic layers, which utilizes spin current injected from the heavy metal by the spin Hall effect to sustain precession in the ferromagnet, benefits from ease of fabrication [26–28]. Moreover, spin Hall nano-oscillators (SHNOs), in the form of a nanoconstriction geometry of these layers, exhibit auto-oscillations by way of mode confinement in a potential well formed by a nonuniform magnetic field [29–31]. Divinskiy *et al.* demonstrated the suppression of nonlinear damping by compensation of in-plane dipolar anisotropy with PMA in Co/Ni-based disks patterned on Pt heavy metal [32]. However, the detection of auto-oscillations is performed by optical methods, which are less suitable for on-chip applications.

Usually, in systems with an interfacial anisotropy, the first-order anisotropy (K_1) dominates over the second-order anisotropy (K_2). However, close to the spin reorientation, when the demagnetization field counterbalances the first-order anisotropy field, K_2 also starts to play a crucial role. In this case, magnetization prefers to align itself along a continuous cone of directions instead of a single axis. The easy cone is exploited to reduce the switching current of magnetic-tunnel-junction- (MTJ) based memory devices [33–35], but a demonstration of an easy cone for the reduction of nonlinearity in SHNOs is still lacking.

Here, we experimentally demonstrate, by all-electrical measurements, a reduction of nonlinearity and linewidth of

an SHNO, based on Co/Ni multilayers with compensated anisotropy and a Pt heavy-metal layer. Compensation is achieved by tuning the thicknesses of the Co/Ni multilayers. The effective anisotropy is estimated using spin-diode measurements performed on microstrip waveguides. The relationship between the second- and first-order anisotropy terms indicate the presence of an easy-cone state, which validates the existence of compensation. The compensated spin diode thus obtained does not show variation of its frequency with the injected rf power and can potentially function as a synapse. Nanoconstriction-based SHNOs with different widths are then patterned on the compensated stacks and the output microwave spectra are analyzed. The frequency is found to remain nearly constant as a function of dc current for a wide range of magnetic field strengths and orientations. Moreover, an extremely low linewidth close to 1 MHz (quality factor = 7500) is obtained, which does not increase significantly at large applied dc currents. In contrast, as a control, an SHNO is fabricated with an in-plane-anisotropy Ni₈₁Fe₁₉/Pt stack, which exhibits a significant shift of frequency and linewidth with applied dc current.

II. COMPENSATION OF ANISOTROPY IN SPIN HALL DEVICES

A. Sample preparation

The stacks consisting of Ta(5)/Pt(6)/[Co(x)/Ni(y)]₅/Co(x)/Al(2) (thicknesses are in nm) are deposited on high-resistivity silicon (001) substrates (resistivity >10 000 Ω cm) by dc magnetron sputtering at room temperature. Ta is used as a seed layer to promote adhesion between silicon and the subsequent layer, and Pt serves as the heavy-metal layer. Co/Ni multilayers are chosen for their large PMA and spin polarization, which can be tuned by varying layer thicknesses [36], as demonstrated previously for domain-wall-based devices [37,38]. A Co/Ni multilayer repetition of five is chosen to obtain a sizeable absolute magnetization [39].

Thicknesses of Co(x) and Ni(y) are varied to tune the anisotropy, and the corresponding M - H loops are measured for in-plane (IP) and out-of-plane (OOP) field orientations using alternating-gradient force magnetometry (AGFM). Starting with in-plane anisotropy (IPA) for Co(0.5 nm) and Ni(0.8 nm) [Fig. 1(a)], the thickness of Co is reduced to 0.4 nm and PMA is obtained [Fig. 1(c)] due to interfacial anisotropy overcoming the demagnetization field. Henceforth, in this article, Co(0.5 nm)/Ni(0.8 nm) and Co(0.4 nm)/Ni(0.8 nm) multilayers are referred to as IPA and PMA stacks, respectively. Furthermore, when the thickness of Ni is increased to 0.9 nm, the PMA reduces, but the anisotropy is neither fully in plane nor out of plane [Fig. 1(b)]. As described in what follows, the intermediate anisotropy obtained with Co(0.4 nm) and Ni(0.9 nm) is compensated for and this film is referred

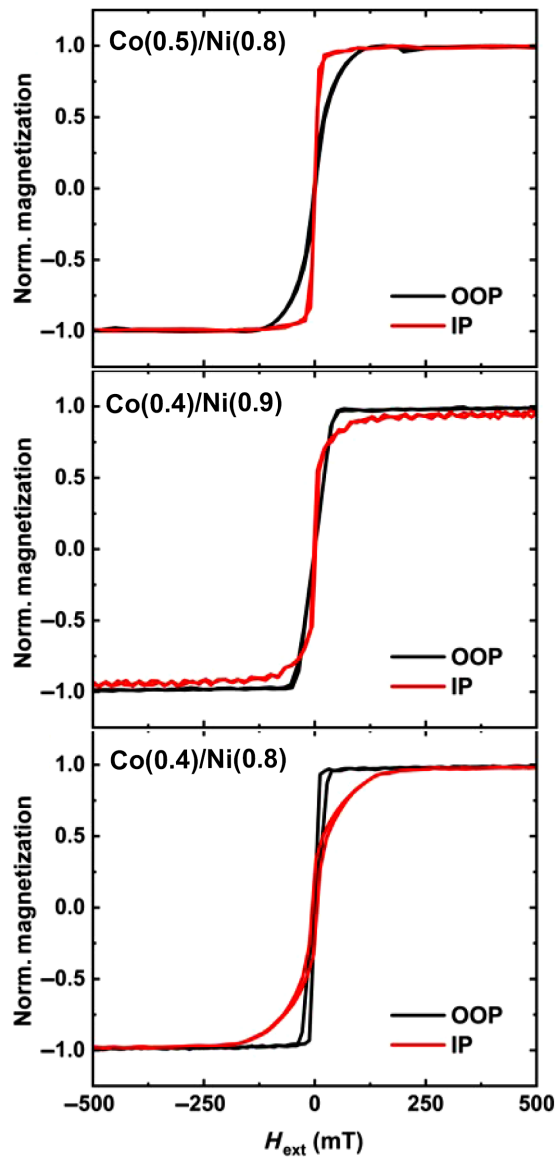


FIG. 1. Alternating-gradient magnetometry measurements for Ta(5)/Pt(6)/[Co(x)/Ni(y)]₅/Co(x)/Al(2) (thicknesses are in nm) films with (a) in-plane anisotropy ($x = 0.5$, $y = 0.8$), (b) compensated anisotropy ($x = 0.4$, $y = 0.9$), and (c) perpendicular anisotropy ($x = 0.4$, $y = 0.8$).

to as the compensated stack. The anisotropy fields are extracted using spin-diode measurements [27,40]. To carry out the measurements, the multilayers are patterned into microstrip waveguides of 10 μm wide and 25 μm long using optical lithography and Ar-ion beam-etching techniques. Ti(15 nm)/Au(150 nm) metal stacks are deposited as electrodes and patterned into coplanar waveguides overlaying the microstrips using optical lithography and lift-off techniques. The resulting samples are henceforth referred to as IPA, PMA, and compensated devices, respectively.

B. Spin-diode measurements and estimation of effective anisotropy

Figure 2 shows the spin-diode measurement setup. A microwave current with a power of 8 mW (9 dBm) is injected into the microstrip device to generate microwave-frequency spin-orbit torque (SOT) on the ferromagnetic layers due to heavy-metal Pt [27]. The mixing between the oscillating magnetoresistance and the microwave current produces a dc rectified voltage, V_{dc} , at the ferromagnetic resonance, which is detected by using a lock-in amplifier. The external field is swept close to the OOP direction for the PMA device ($\theta = 5^\circ$) and is swept IP ($\varphi = 45^\circ$) for the compensated and IPA devices, where θ and φ are the polar and azimuthal angles, respectively. By keeping the field orientation close to the anisotropy of the devices, we can eliminate artefacts due to geometry-induced local anisotropy variation and simplify the analysis [41]. All measurements are performed at room temperature. Resonance plots obtained for the PMA, compensated, and IPA devices are shown in Figs. 3(a)–3(c), respectively. The amplitudes observed in the resonance plots are not corrected for the nonflat frequency response of the wire bonds and the cabling in the setup. However, in our analysis, we are only interested in the estimation of the resonance fields that are independent of amplitude losses. The plots can be well fitted by the sum of symmetric and antisymmetric Lorentzian curves [27]. The resonance field, H_r , is extracted for each of the injected microwave frequencies (f_{res}), and the Kittel functions (f_{res} vs H_r) are plotted for each of the three configurations. The linear relationship obtained in Fig. 3(d) for the PMA device is well explained by the Kittel formula, $f_{\text{res}} = \gamma/2\pi(H_r - \mu_0 M_{\text{eff}})$ [42], where $\mu_0 M_{\text{eff}} = \mu_0 M_s - H_k$ is the effective anisotropy field; symbols γ , μ_0 , M_s , and H_k denote the gyromagnetic ratio, vacuum permeability, saturation magnetization, and perpendicular anisotropy field, respectively. Fitting of the equation yields $M_{\text{eff}} = -35$ mT. The negative sign of M_{eff} confirms the existence of PMA. Figures 3(e)

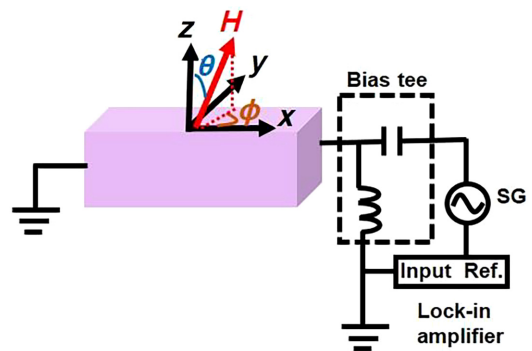


FIG. 2. Schematic illustration of spin-diode measurement setup.

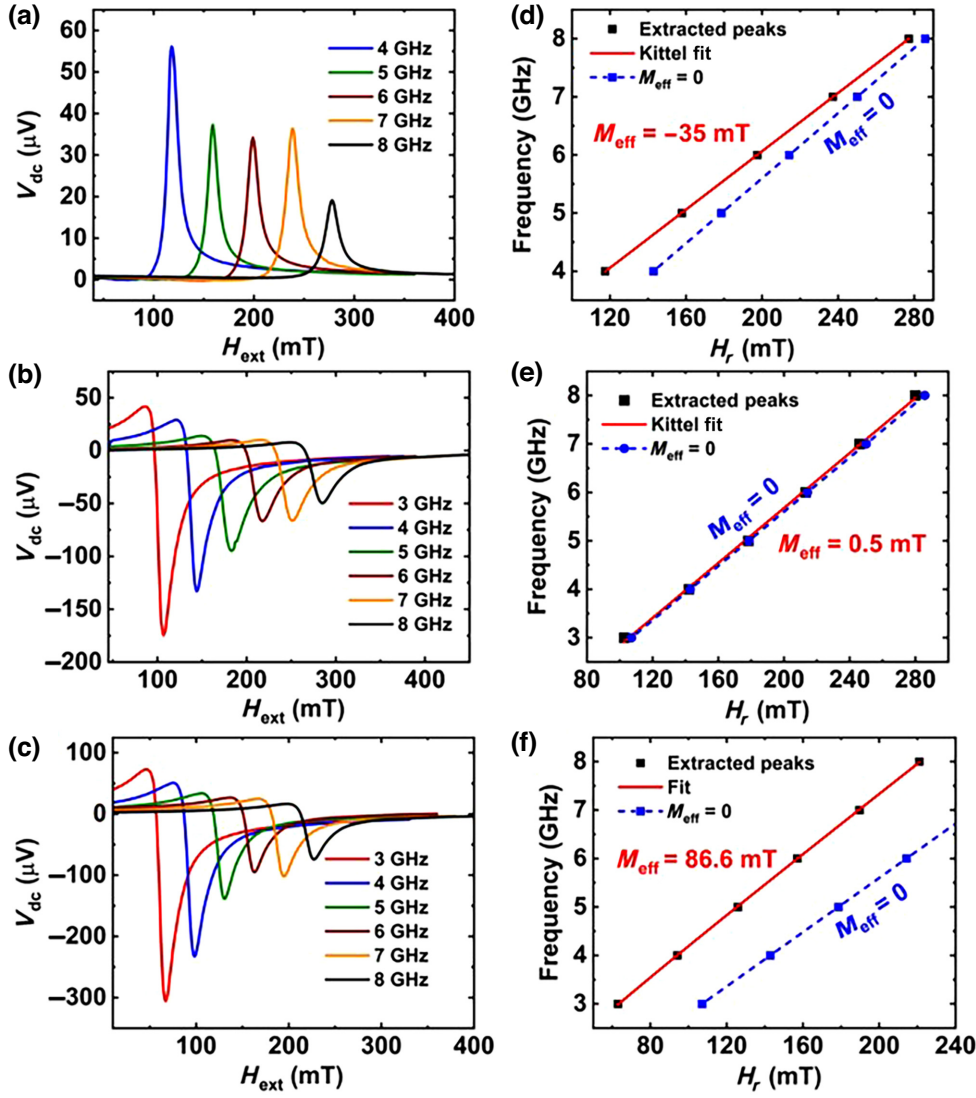


FIG. 3. Spin-diode resonance plots at different injected microwave frequencies for (a) PMA, (b) compensated, and (c) IPA-stack-based microstrip waveguides. Resonance frequency as a function of the resonance field for (d) PMA, (e) compensated, and (f) IPA-stack-based microstrip waveguides. Solid red lines are Kittel fits, and dotted blue lines, plotted for guidance, correspond to $M_{\text{eff}}=0$.

and 3(f) depict the f_{res} versus H_r plots for the compensated and IPA devices, respectively, which are well fitted with the equation $f_{\text{res}} = \gamma/2\pi [H_r(H_r + \mu_0 M_{\text{eff}})]^{1/2}$ [27]. The extracted values of M_{eff} are $+0.5$ and $+86.6$ mT for the compensated and the IPA devices, respectively. As a comparison, the Kittel function corresponding to $M_{\text{eff}}=0$ is also plotted together with the as-obtained fits for each of the three devices. Clearly, the compensated stack-based device is closest to the near-zero effective anisotropy.

Given that the first-order anisotropy is close to zero in the compensated device, the possible influence of the second-order anisotropy needs to be taken into consideration. The following equations are the more generalized forms, which take the second-order anisotropy into consideration:

$$f = \gamma/2\pi (H_1 H_2)^{1/2}, \quad (3)$$

with

$$\begin{aligned} H_1 &= H_r \cos(\theta_H - \theta_M) + H_{k_1}^{\text{eff}} \cos^2 \theta_M - H_{k_2} \cos^4 \theta_M, \\ H_2 &= H_r \cos(\theta_H - \theta_M) + H_{k_1}^{\text{eff}} \cos 2\theta_M \\ &\quad - H_{k_2}/2(\cos 2\theta_M + \cos 4\theta_M), \end{aligned} \quad (4)$$

where θ_H and θ_M correspond to the angle of the external magnetic field and the magnetization angle measured from the sample normal, respectively. $H_{k_1}^{\text{eff}}$ and H_{k_2} correspond to the first- and second-order effective-anisotropy fields, respectively [43]. By adopting $H_{k_1}^{\text{eff}}$, H_{k_2} , and γ as adjustable parameters, the θ_H dependence of H_r yields the first- and second-order anisotropy fields. The energy-minimum conditions, $\partial F/\partial \theta_M = 0$ and $\partial^2 F/\partial \theta_M^2 > 0$, are used to extract the value for θ_M , where F is the magnetic energy density [43].

Spin-diode measurements are performed by sweeping the magnetic field at different out-of-plane angles, θ_H ,

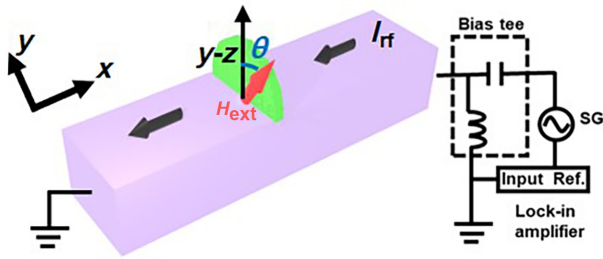


FIG. 4. Schematic illustration of spin-diode measurement setup when the external field is rotated out of plane.

in the y - z plane, as shown in the schematic of Fig. 4. In this geometry, the signal strength of the output voltage is larger due to the spin-pumping contributions [44]. The resonance fields, H_r , are extracted from the sum of symmetric and antisymmetric Lorentzians for each of the angles. The measurements are first performed for the IPA and PMA devices. The extracted H_r as a function of θ_H is shown in Figs. 5(a) and 5(b), with input microwave frequencies fixed at 3 and 4 GHz for the IPA and PMA devices, respectively. The curves display monotonic behavior, where H_r is minimum close to the in-plane angle ($\theta_H = \pm 90^\circ$) for the IPA device and close to the out-of-plane angle ($\theta_H = 0^\circ$) for the PMA device. The nature of the curves is independent of the input microwave frequency; different values are selected for the two devices based on the signal quality. The measurements are performed at a frequency of 5 GHz for the compensated device, and the corresponding H_r versus θ_H plot is shown in Fig. 5(c). The curve display nonmonotonic behavior, where H_r is minimum at an intermediate angle close to 50° . This is referred to as the cone angle, and its existence is an indication of compensation of anisotropy [34,45]. The curves are well fitted with Eq. (4) and are used to extract $H_{k_1}^{\text{eff}} = -0.8$ mT and $H_{k_2} = 0.47$ mT. The obtained parameters also satisfy the following conditions for the existence of an easy cone: $H_{k_1}^{\text{eff}} < 0$; $H_{k_2} > 0$ and $H_{k_2} >$

$-H_{k_1}^{\text{eff}}/2$ [34]. These measurements thus demonstrate that a device with compensated anisotropy is fabricated. It can be further employed to demonstrate fixed-frequency applications.

C. Input-independent spin Hall diode with fixed frequency

A synapse can be realized using spin diodes. Leroux *et al.* demonstrated a MAC operation using magnetic tunnel junctions as spin diodes [22]. In a MAC operation, the output voltage, U_j , can be represented by a weighted sum of the input power, $U_j = \sum P_i W_{ji}$. This equation can be mapped to a spin-diode equation in the linear zone close to resonance, where the weights are represented by the resonator frequencies. During frequency multiplexing in a MAC operation, each injected input power, P_i , should be able to uniquely address the corresponding synapse by its frequency. This imposes a constraint on the frequency of the resonator. This criterion is usually not satisfied, on account of the inherent nonlinearity. However, the compensated spin diode has the potential to function as an input-independent synapse with a fixed frequency. Figure 6(a) shows the shift in H_r as a function of the injected input rf power for the IPA, compensated, and PMA spin diodes. Starting at the minimum input power ($=1$ mW), the shift is normalized to zero for all the three devices. As the input power is increased, the IPA and PMA devices exhibit an increase in the shift of H_r , whereas the compensated device shows a negligible shift in H_r . Figures 6(b) and 6(c) show a comparison of the resonance plots for the IPA and compensated devices, respectively, as a function of the input power. Clearly, there is no visible shift in the resonance field and the equivalent frequency with the injected rf power for the compensated device compared to the IPA device. Thus, the compensated spin diode has the potential to function as an input-independent spin Hall synapse.

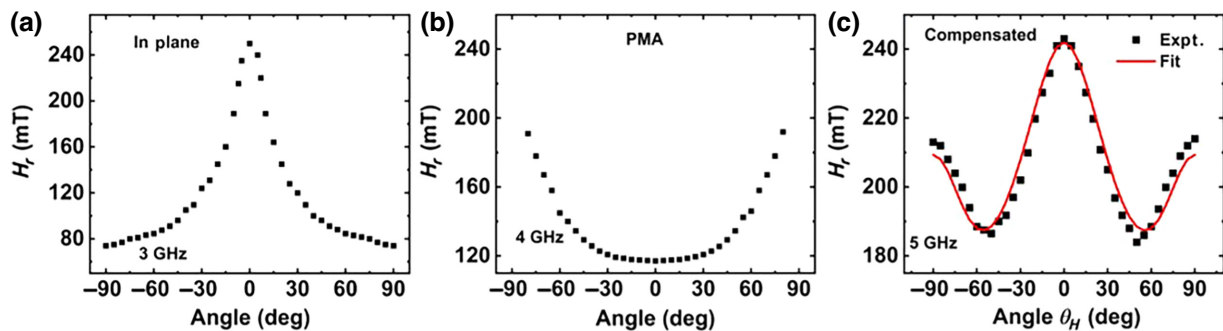


FIG. 5. Resonance field versus field angle for the microstrip waveguide with (a) IPA stack, microwave frequency fixed at 3 GHz; (b) PMA stack, microwave frequency fixed at 4 GHz; and (c) compensated stack, microwave frequency fixed at 5 GHz.

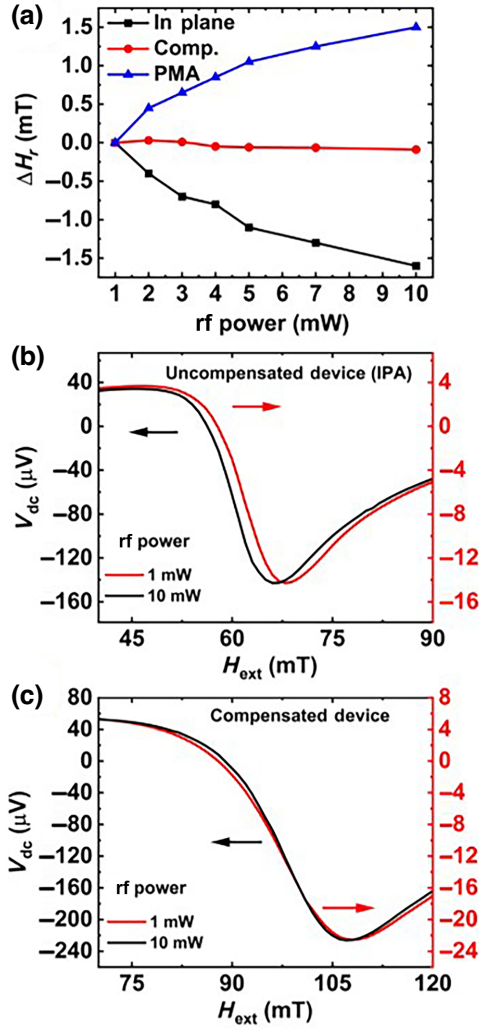


FIG. 6. (a) Comparison of shift in resonance field as a function of input rf power for a spin diode in IPA, compensated, and PMA configuration. Resonance curves as a function of input rf power for (b) IPA and (c) compensated (synapse) spin diodes.

III. AUTO-OSCILLATIONS IN COMPENSATED SPIN HALL DEVICES: FIXED FREQUENCY AND LOW LINWIDTH

A. Device fabrication and measurement setup

Nanoconstrictions with widths of 100 and 200 nm are fabricated on the compensated Co/Ni stacks using electron-beam lithography and Ar-ion beam etching. Ti(15 nm)/Au(150 nm) metal stacks are deposited as electrodes and patterned into coplanar waveguides overlaying the nanoconstrictions using optical lithography and lift-off. The device geometry is similar to the one used in previous reports for realizing an SHNO [30,31]. As a comparison, an in-plane SHNO based on Py/Pt stacks is also patterned into nanoconstrictions (Py = Permalloy = $\text{Ni}_{81}\text{Fe}_{19}$).

The scanning electron microscopy image of a 200-nm nanoconstriction, along with the measurement setup to

detect the auto-oscillations, is shown in Fig. 7(a). A dc current, I_{dc} , is injected into the nanoconstriction via the dc port of a bias tee. An external magnetic field is applied at an in-plane angle, ϕ_H , and an out-of-plane angle, θ_H . The SHNO emits microwave power, which is extracted from the rf port of the bias tee and amplified by 38 dB using a low-noise wideband amplifier. The output spectra are sampled using a spectrum analyzer. All measurements are performed at room temperature.

B. Electrical microwave measurements for compensated and in-plane devices

Figure 7(b) shows the emission spectra for the 200-nm SHNO realized using the compensated Co/Ni stack at $I_{dc} = -2.8$ mA (+x direction) and $H_{ext} = 300$ mT ($\theta_H = 15^\circ$, $\phi_H = 50^\circ$). The linewidth (Δf) obtained from the Lorentz fit is 1.1 MHz with a peak power spectral density (PSD), after subtracting the amplifier gain, as high as 1 pW/MHz. The quality factor ($Q \approx 7500$) obtained is higher than that reported using a single-constriction-based SHNO [18,46]. As a comparison, the above measurements are also performed on Py/Pt-based SHNO devices. Figure 7(c) shows the corresponding spectra obtained at $I_{dc} = +3.5$ mA and $H_{ext} = 50$ mT ($\theta_H = 85^\circ$, $\phi_H = 42^\circ$). The field orientation is maintained close to the in-plane direction for this device to excite the in-plane modes. In this case, the sign of I_{dc} is positive, as the SOT is from the top interface, whereas for the Pt/Co/Ni multilayers the sign of I_{dc} is negative, since the SOT is from the bottom interface. The minimum linewidth obtained from the Lorentz fit is 7.85 MHz and is much larger than that achieved using the compensated Co/Ni SHNO. The above observations can be explained from Eq. (2), which indicates a reduction of Δf if N is reduced. To further validate this claim, we sweep the injected I_{dc} and record the variation of the frequency and Δf for the two SHNOs at the abovementioned external fields and orientations, respectively. Figures 7(d) and 7(e) show Δf as a function of I_{dc} for the compensated Co/Ni and in-plane Py/Pt SHNOs, respectively. Figure 7(d) is plotted for I_{dc} larger than the critical current of auto-oscillations ($I_c = -2.7$ mA), which is the region of interest, and the inset shows data for $I < I_c$ as well. When $I_{dc} < I_c$, Δf increases with the reduction in current for both devices, as expected. At large I_{dc} , the Py/Pt SHNO shows an increase in Δf due to the inherent nonlinearity, which is not the case with the compensated Co/Ni SHNO, which shows a near-constant Δf . Evidence for the absence of nonlinearity in the compensated Co/Ni SHNO becomes stronger when we compare its frequency versus I_{dc} shown in the power spectral density plot in Fig. 7(f) to that obtained for Py/Pt SHNO in Fig. 7(g). Clearly, the rate of change of frequency with current (df/dI) is minimal for the compensated Co/Ni SHNO ($=10$ MHz/mA) and significant for the in-plane Py/Pt

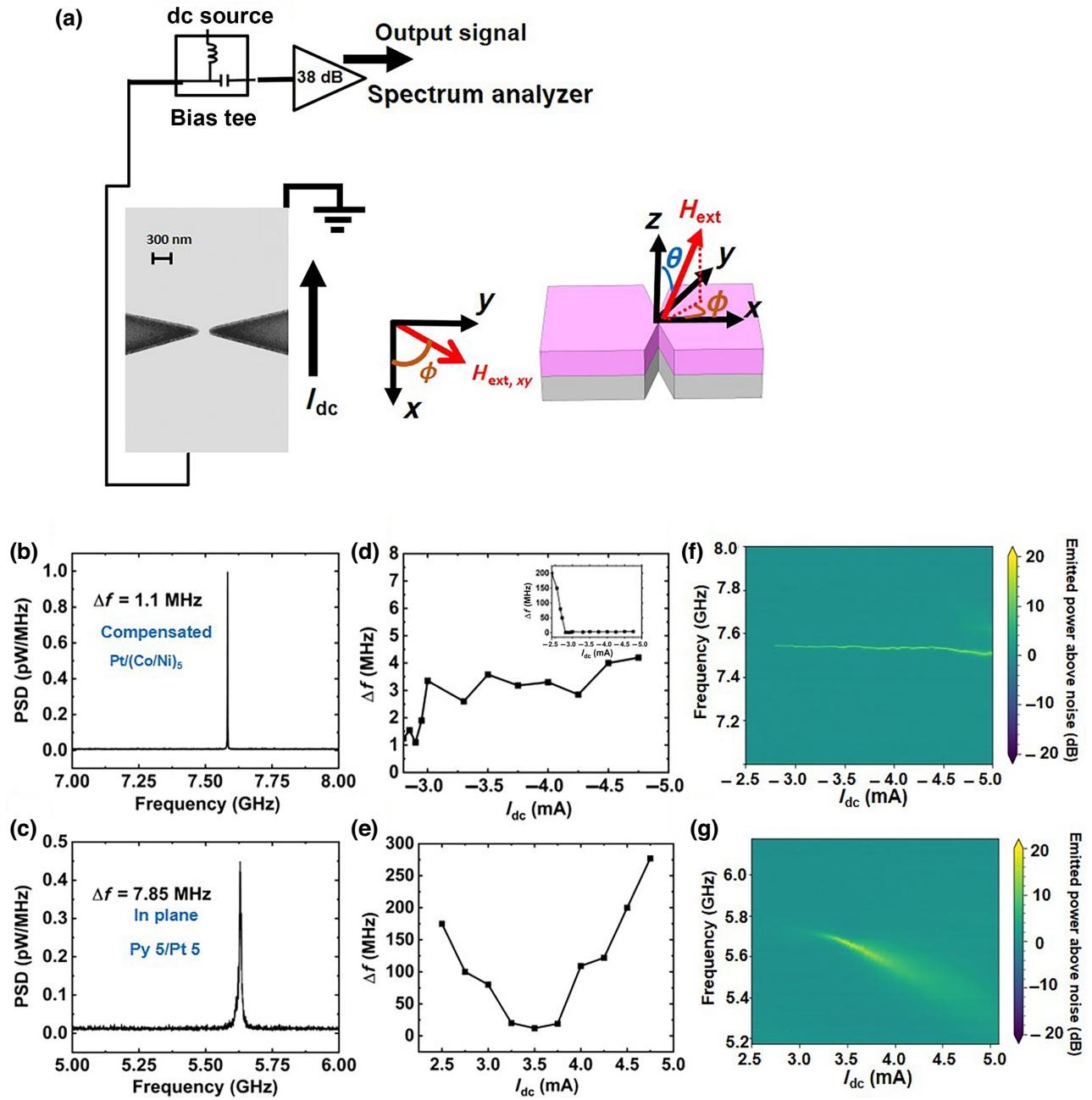


FIG. 7. (a) SEM image of 200-nm nanoconstriction, and a schematic to study microwave emission from the SHNO. (b) Auto-oscillation spectra for the compensated Co/Ni SHNO obtained at $I_{dc} = +2.8$ mA, $H_{ext} = 300$ mT ($\theta_H = 15^\circ$, $\phi_H = 50^\circ$). (c) Auto-oscillation spectra for the in-plane Py/Pt SHNO obtained at $I_{dc} = -3.5$ mA, $H_{ext} = 50$ mT ($\theta_H = 85^\circ$, $\phi_H = 42^\circ$). Linewidth as a function of I_{dc} sweep for (d) compensated Co/Ni SHNO and (e) in-plane Py/Pt SHNO. Power spectral density plots showing frequency versus I_{dc} sweep for (f) compensated Co/Ni SHNO and (g) in-plane Py/Pt SHNO.

SHNO (≈ 500 MHz/mA). However, for $I_{dc} > -4.5$ mA, some nonlinearity can be observed in Fig. 7(f), which can be ascribed to the device heating or frequency shift due to the Oersted field or the fieldlike torque [39]. The above observations are a direct validation of a reduction in nonlinearity, as indicated in Eq. (1). The measurements are repeated at different applied external magnetic fields to the

compensated Co/Ni SHNO and are shown in Fig. 8. As is the case, the external fields change only the frequency of the ferromagnetic resonance and not the slope, which is nearly zero for the compensated Co/Ni SHNO.

To further validate the existence of compensation across different devices, the measurements are repeated on a 100-nm constriction. Figure 9(a) shows the variation of Δf

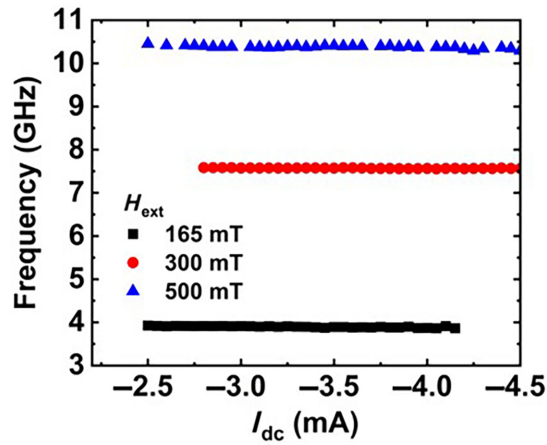


FIG. 8. Auto-oscillation frequency as a function of I_{dc} sweep for compensated Co/Ni SHNO performed at external fields of 165, 300, and 500 mT.

versus I_{dc} for this device, performed at $H_{ext}=180$ mT ($\theta_H = 15^\circ$, $\phi_H = 50^\circ$). The plot indicates a high Δf for $I_{dc} < I_c$ ($= -1.8$ mA), as shown in the inset, after which it does not increase significantly at higher currents. A larger Δf in excess of 5 MHz, as opposed to 1.1 MHz, is obtained when the width of the constriction is reduced from 200 to 100 nm, which is expected due to a smaller mode volume. We also perform frequency versus I_{dc} for this device at different orientations of the external magnetic field ($H_{ext}=180$ mT). The measurements are performed for three different angles, $\theta_H = 22^\circ$, 30° , and 46° , keeping ϕ_H fixed at 90° . Figure 9(b) shows the results of frequency versus I_{dc} at different out-of-plane angles of the external field. At each angle, the frequency is different, as expected, and is minimum at 46° , which is close to the cone angle of precession. However, the frequency remains nearly constant with respect to I_{dc} , even at different angles, thus providing strong evidence for the absence of nonlinearity in the compensated SHNO device.

The results above highlight notable differences in device properties and oscillation conditions for the 200- and 100-nm-wide nanoconstrictions. These variations in width lead to distinct internal fields due to geometry- and fabrication-related variability. Factors such as shape-induced anisotropy modification and etch-induced

reduction of PMA affect smaller nanoconstrictions more significantly [47]. Consequently, different fields and applied angles alter the effective fields, resulting in dissimilar oscillation frequencies for the two widths. Furthermore, the effective anisotropy for nanoconstriction geometries of varying widths would also differ.

In a previous estimation, M_{eff} for the micron-sized device was calculated to be 0.5 mT [Fig. 3(e)]. To estimate M_{eff} in nanoconstrictions, we conduct spin-diode measurements on the 100- and 200-nm nanoconstrictions using the

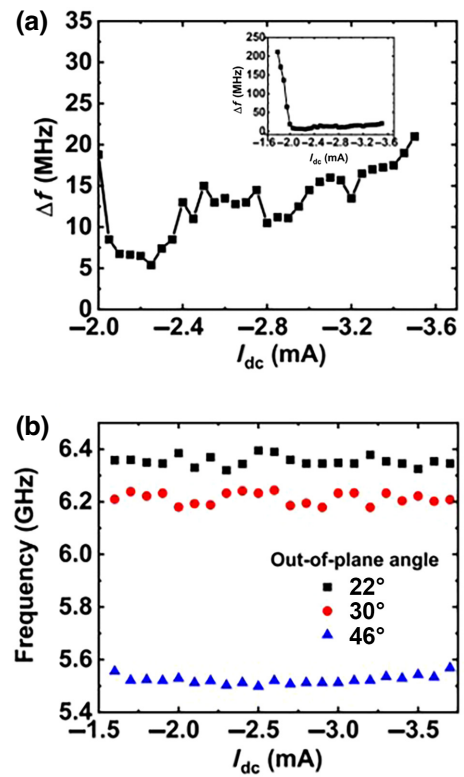


FIG. 9. (a) Linewidth as a function of I_{dc} sweep at $H_{ext}=180$ mT ($\theta_H = 15^\circ$, $\phi_H = 50^\circ$) for the 100-nm-wide compensated Co/Ni SHNO. (b) Comparison of frequency versus I_{dc} sweep when $H_{ext}=180$ mT is applied along out-of-plane angles of 22° , 30° , and 46° to the 100-nm compensated Co/Ni SHNO.

methods outlined in Ref. [48]. The M_{eff} values are determined to be +9.4 and +5.2 mT for 100- and 200-nm nanoconstrictions, respectively. As anticipated, these values are significantly larger than the estimated value for the microstrip (0.5 mT). The positive sign suggests a reduction of PMA, with the 100-nm nanoconstriction exhibiting weaker PMA. Nevertheless, the effective anisotropy remains an order of magnitude lower than previously reported values [48] and continues to display reduced frequency tunability with current.

It should be noted that data presented for minimum linewidths represent the best device obtained. However, factors such as device-to-device variability, as previously discussed, and fabrication process artifacts can also influence the minimum linewidths across different devices with the same widths. Furthermore, Joule heating and current-induced Oersted fields could impact the results. We conduct measurements for five different devices for each nominal width of the nanoconstriction, with details provided in the Supplemental Material [49]. The linewidth for the 100-nm nanoconstriction is determined to be (6.2 ± 1.8) MHz, while for the 200-nm nanoconstriction it is found to be (1.8 ± 0.6) MHz. Although the effects of device-to-device

variability are more pronounced near anisotropy compensation, the obtained linewidths are considerably lower than those reported for uncompensated Co/Ni-based PMA oscillator devices [31,50].

IV. CONCLUSION

Here, we experimentally demonstrate a significant reduction of nonlinearity in the magnetization dynamics of an SHNO by compensating for its effective magnetic anisotropy using Co/Ni multilayers with a Pt heavy metal. By tuning the thicknesses of Co and Ni, we are able to obtain an easy-cone anisotropy for the compensated stack when the perpendicular magnetic anisotropy is counterbalanced by the demagnetization field. The spin-diode signal is shown to be independent of the input power, making it a promising candidate for synapses in neuromorphic computing applications.

We also investigate auto-oscillations in the compensated SHNO using nanoconstrictions and compare them with Py/Pt-based SHNOs with an in-plane anisotropy. Our results demonstrate that the frequency and linewidth of the compensated SHNO are independent of the applied dc current, external fields, and orientations, with a linewidth as low as 1.1 MHz and a peak emission power as high as 1 pW/MHz. This indicates the possibility of realizing nano-oscillators with improved device performance, potentially reducing phase noise by decoupling amplitude noise from it.

Our study also opens up possibilities for neuromorphic applications, such as frequency multiplexing in a multiply-and-accumulate operation. The compensated SHNO can function as a neuron of low linewidth and a fixed frequency, uniquely addressing a compensated spin diode as a synapse. Additionally, it opens up prospects for generating voltage spikes that emulate spike-based neurons by exploiting easy-plane oscillations in a compensated SHNO. These findings suggest exciting prospects for the development of neuromorphic devices with improved performance and functionality.

ACKNOWLEDGMENTS

This work is supported by the Agence Nationale de la Recherche Project ANR-20-CE24-0002 (SpinSpike). J.G. and D.H.S. acknowledge support from Q-MEEN-C, an Energy Frontier Research Center funded by the U.S. Department of Energy, Office of Science, Basic Energy Science, under Grant No. DE-SC0019273, for work on neuromorphic computing with SHNO.

[1] J. C. Slonczewski, Current-driven excitation of magnetic multilayers, *J. Magn. Mater.* **159**, L1 (1996).

- [2] L. Berger, Emission of spin waves by a magnetic multilayer traversed by a current, *Phys. Rev. B* **54**, 9353 (1996).
- [3] S. I. Kiselev, J. C. Sankey, I. N. Krivorotov, N. C. Emley, R. J. Schoelkopf, R. A. Buhrman, and D. C. Ralph, Microwave oscillations of a nanomagnet driven by a spin-polarized current, *Nature* **425**, 380 (2003).
- [4] V. E. Demidov, S. Urazhdin, H. Ulrichs, V. Tiberkevich, A. Slavin, D. Baither, G. Schmitz, and S. O. Demokritov, Magnetic nano-oscillator driven by pure spin current, *Nat. Mater.* **11**, 1028 (2012).
- [5] A. Slavin and V. Tiberkevich, Nonlinear auto-oscillator theory of microwave generation by spin-polarized current, *IEEE Trans. Magn.* **45**, 1875 (2009).
- [6] A. N. Slavini and P. Kabos, Approximate theory of microwave generation in a current-driven magnetic nanocontact magnetized in an arbitrary direction, *IEEE Trans. Magn.* **41**, 1264 (2005).
- [7] M. Dvornik, A. A. Awad, and J. Åkerman, Origin of Magnetization Auto-Oscillations in Constriction-Based Spin Hall Nano-Oscillators, *Phys. Rev. Appl.* **9**, 014017 (2018).
- [8] M. Zahedinejad, A. A. Awad, P. Dürrenfeld, A. Houshang, Y. Yin, P. K. Muduli, and J. Åkerman, Current modulation of nanoconstriction spin-Hall nano-oscillators, *IEEE Magn. Lett.* **8**, 1 (2017).
- [9] P. K. Muduli, Ye. Pogoryelov, S. Bonetti, G. Consolo, F. Mancoff, and J. Åkerman, Nonlinear frequency and amplitude modulation of a nanocontact-based spin-torque oscillator, *Phys. Rev. B* **81**, 140408 (2010).
- [10] M. R. Pufall, W. H. Rippard, S. Kaka, T. J. Silva, and S. E. Russek, Frequency modulation of spin-transfer oscillators, *Appl. Phys. Lett.* **86**, 082506 (2005).
- [11] A. Litvinenko, A. Sidi El Valli, V. Iurchuk, S. Louis, V. Tyberkevych, B. Dieny, A. N. Slavin, and U. Ebels, Ultrafast GHz-range swept-tuned spectrum analyzer with 20 ns temporal resolution based on a spin-torque nano-oscillator with a uniformly magnetized “free” layer, *Nano Lett.* **22**, 1874 (2022).
- [12] A. Litvinenko, P. Sethi, C. Murapaka, A. Jenkins, V. Cros, P. Bortolotti, R. Ferreira, B. Dieny, and U. Ebels, Analog and Digital Phase Modulation and Signal Transmission with Spin-Torque Nano-Oscillators, *Phys. Rev. Appl.* **16**, 024048 (2021).
- [13] A. Litvinenko, V. Iurchuk, P. Sethi, S. Louis, V. Tyberkevych, J. Li, A. Jenkins, R. Ferreira, B. Dieny, A. Slavin, and U. Ebels, Ultrafast sweep-tuned spectrum analyzer with temporal resolution based on a spin-torque nano-oscillator, *Nano Lett.* **20**, 6104 (2020).
- [14] R. Sharma, R. Mishra, T. Ngo, Y. X. Guo, S. Fukami, H. Sato, H. Ohno, and H. Yang, Electrically connected spin-torque oscillators array for 2.4 GHz WiFi band transmission and energy harvesting, *Nat. Commun.* **12**, 2924 (2021).
- [15] H. S. Lee, S. H. Kim, T. H. Jang, H. G. Park, B. C. Min, S. Y. Park, and C. S. Park, Power-efficient spin-torque nano-oscillator-based wireless communication with CMOS high-gain low-noise transmitter and receiver, *IEEE Trans. Magn.* **55**, 1 (2019).
- [16] S. Tsunegi, T. Taniguchi, K. Nakajima, S. Miwa, K. Yakushiji, A. Fukushima, S. Yuasa, and H. Kubota, Physical reservoir computing based on spin torque oscillator with forced synchronization, *Appl. Phys. Lett.* **114**, 164101 (2019).

- [17] M. Romera, P. Talatchian, S. Tsunegi, K. Yakushiji, A. Fukushima, H. Kubota, S. Yuasa, V. Cros, P. Bortolotti, M. Ernoult, D. Querlioz, and J. Grollier, Binding events through the mutual synchronization of spintronic nano-neurons, *Nat. Commun.* **13**, 883 (2022).
- [18] M. Zahedinejad, A. A. Awad, S. Muralidhar, R. Khymyn, H. Fulara, H. Mazraati, M. Dvornik, and J. Åkerman, Two-dimensional mutually synchronized spin Hall nano-oscillator arrays for neuromorphic computing, *Nat. Nanotechnol.* **15**, 47 (2020).
- [19] M. Romera, P. Talatchian, S. Tsunegi, F. A. Araujo, V. Cros, P. Bortolotti, J. Trastoy, K. Yakushiji, A. Fukushima, H. Kubota, S. Yuasa, M. Ernoult, D. Vodenicarevic, T. Hirtzlin, N. Locatelli, D. Querlioz, and J. Grollier, Vowel recognition with four coupled spin-torque nano-oscillators, *Nature* **563**, 230 (2018).
- [20] D. C. Ralph and M. D. Stiles, Spin transfer torques, *J. Magn. Magn. Mater.* **320**, 1190 (2008).
- [21] A. Ross, *et al.*, Multilayer spintronic neural networks with radio-frequency connections, ArXiv Preprint ArXiv:2211.03659 (2022).
- [22] N. Leroux, D. Marković, E. Martin, T. Petrisor, D. Querlioz, A. Mizrahi, and J. Grollier, Radio-Frequency Multiply-and-Accumulate Operations with Spintronic Synapses, *Phys. Rev. Appl.* **15**, 034067 (2021).
- [23] M. W. Keller, M. R. Pufall, W. H. Rippard, and T. J. Silva, Nonwhite frequency noise in spin torque oscillators and its effect on spectral linewidth, *Phys. Rev. B* **82**, 54416 (2010).
- [24] D. Marković, M. W. Daniels, P. Sethi, A. D. Kent, M. D. Stiles, and J. Grollier, Easy-plane spin Hall nano-oscillators as spiking neurons for neuromorphic computing, *Phys. Rev. B* **105**, 014411 (2022).
- [25] S. Jiang, R. Khymyn, S. Chung, T. Q. Le, L. H. Diez, A. Houshang, M. Zahedinejad, D. Ravelosona, and J. Åkerman, Reduced spin torque nano-oscillator linewidth using He⁺ irradiation, *Appl. Phys. Lett.* **116**, 072403 (2020).
- [26] E. Saitoh, M. Ueda, H. Miyajima, and G. Tatara, Conversion of spin current into charge current at room temperature: Inverse spin-Hall effect, *Appl. Phys. Lett.* **88**, 182509 (2006).
- [27] L. Liu, T. Moriyama, D. C. Ralph, and R. A. Buhrman, Spin-Torque Ferromagnetic Resonance Induced by the Spin Hall Effect, *Phys. Rev. Lett.* **106**, 36601 (2011).
- [28] J. E. Hirsch, Spin Hall Effect, *Phys. Rev. Lett.* **83**, 1834 (1999).
- [29] H. Mazraati, S. Chung, A. Houshang, M. Dvornik, L. Piazza, F. Qejvanaj, S. Jiang, T. Q. Le, J. Weissenrieder, and J. Åkerman, Low operational current spin Hall nano-oscillators based on NiFe/W bilayers, *Appl. Phys. Lett.* **109**, 242402 (2016).
- [30] V. E. Demidov, S. Urazhdin, A. Zholud, A. v. Sadovnikov, and S. O. Demokritov, Nanoconstriction-based spin-Hall nano-oscillator, *Appl. Phys. Lett.* **105**, 172410 (2014).
- [31] B. Divinskiy, V. E. Demidov, A. Kozhanov, A. B. Rinkevich, S. O. Demokritov, and S. Urazhdin, Nanoconstriction spin-Hall oscillator with perpendicular magnetic anisotropy, *Appl. Phys. Lett.* **111**, 032405 (2017).
- [32] B. Divinskiy, S. Urazhdin, S. O. Demokritov, and V. E. Demidov, Controlled nonlinear magnetic damping in spin-Hall nano-devices, *Nat. Commun.* **10**, 5211 (2019).
- [33] A. A. Timopheev, R. Sousa, M. Chshiev, H. T. Nguyen, and B. Dieny, Second order anisotropy contribution in perpendicular magnetic tunnel junctions, *Sci. Rep.* **6**, 26877 (2016).
- [34] A. Okada, S. Kanai, S. Fukami, H. Sato, and H. Ohno, Electric-field effect on the easy cone angle of the easy-cone state in CoFeB/MgO investigated by ferromagnetic resonance, *Appl. Phys. Lett.* **112**, 172402 (2018).
- [35] B. M. S. Teixeira, A. A. Timopheev, N. Caçoilo, S. Aufret, R. C. Sousa, B. Dieny, and N. A. Sobolev, Stabilization of the easy-cone magnetic state in free layers of magnetic tunnel junctions, *Phys. Rev. B* **100**, 184405 (2019).
- [36] G. H. O. Daalderop, P. J. Kelly, and F. J. A. den Broeder, Prediction and Confirmation of Perpendicular Magnetic Anisotropy in Co/Ni Multilayers, *Phys. Rev. Lett.* **68**, 682 (1992).
- [37] P. Sethi, C. Murapaka, G. J. Lim, and W. S. Lew, In-plane current induced domain wall nucleation and its stochasticity in perpendicular magnetic anisotropy Hall cross structures, *Appl. Phys. Lett.* **107**, 192401 (2015).
- [38] S. Fukami, Y. Nakatani, T. Suzuki, K. Nagahara, N. Ohshima, and N. Ishiwata, Relation between critical current of domain wall motion and wire dimension in perpendicularly magnetized Co/Ni nanowires, *Appl. Phys. Lett.* **95**, 232504 (2009).
- [39] N. Figueiredo-Prestes, S. Krishnia, S. Collin, Y. Rousigné, M. Belmeguenai, S. M. Chérif, J. Zarpellon, D. H. Mosca, H. Jaffrès, L. Vila, N. Reyren, and J.-M. George, Magnetization switching and deterministic nucleation in Co/Ni multilayered disks induced by spin-orbit torques, *Appl. Phys. Lett.* **119**, 032410 (2021).
- [40] A. A. Tulapurkar, Y. Suzuki, A. Fukushima, H. Kubota, H. Maehara, K. Tsunekawa, D. D. Djayaprawira, N. Watanabe, and S. Yuasa, Spin-torque diode effect in magnetic tunnel junctions, *Nature* **438**, 339 (2005).
- [41] J. G. Choi, J. Park, M. G. Kang, D. Kim, J. S. Rieh, K. J. Lee, K. J. Kim, and B. G. Park, Voltage-driven gigahertz frequency tuning of spin Hall nano-oscillators, *Nat. Commun.* **13**, 3783 (2022).
- [42] J.-M. Beaujour, D. Ravelosona, I. Tudosa, E. E. Fullerton, and A. D. Kent, Ferromagnetic resonance linewidth in ultrathin films with perpendicular magnetic anisotropy, *Phys. Rev. B* **80**, 180415 (2009).
- [43] A. Okada, S. Kanai, M. Yamanouchi, S. Ikeda, F. Matsukura, and H. Ohno, Electric-field effects on magnetic anisotropy and damping constant in Ta/CoFeB/MgO investigated by ferromagnetic resonance, *Appl. Phys. Lett.* **105**, 052415 (2014).
- [44] A. Okada, Y. Takeuchi, K. Furuya, C. Zhang, H. Sato, S. Fukami, and H. Ohno, Spin-Pumping-Free Determination of Spin-Orbit Torque Efficiency from Spin-Torque Ferromagnetic Resonance, *Phys. Rev. Appl.* **12**, 014040 (2019).
- [45] Y. Fu, I. Barsukov, J. Li, A. M. Gonçalves, C. C. Kuo, M. Farle, and I. N. Krivorotov, Temperature dependence of perpendicular magnetic anisotropy in CoFeB thin films, *Appl. Phys. Lett.* **108**, 142403 (2016).

- [46] T. Chen, R. K. Dumas, A. Eklund, P. K. Muduli, A. Houshang, A. A. Awad, P. Dürrenfeld, B. G. Malm, A. Rusu, and J. Åkerman, Spin-torque and spin-Hall nano-oscillators, *Proc. IEEE* **104**, 1919 (2016).
- [47] H. Fulara, M. Zahedinejad, R. Khymyn, A. A. Awad, S. Muralidhar, M. Dvornik, and J. Åkerman, Spin-orbit torque-driven propagating spin waves, *Sci. Adv.* **5**, 1 (2019).
- [48] H. Fulara, M. Zahedinejad, R. Khymyn, M. Dvornik, S. Fukami, S. Kanai, H. Ohno, and J. Åkerman, Giant voltage-controlled modulation of spin Hall nano-oscillator damping, *Nat. Commun.* **11**, 4006 (2020).
- [49] See the Supplemental Material at <http://link.aps.org/supplemental/10.1103/PhysRevApplied.19.064018> for linewidth variation across different devices for the same width of nanoconstrictions.
- [50] R. H. Liu, W. L. Lim, and S. Urazhdin, Dynamical Skyrmion State in a Spin Current Nano-Oscillator with Perpendicular Magnetic Anisotropy, *Phys. Rev. Lett.* **114**, 137201 (2015).